ELSEVIER

Polymer 41 (2000) 1827–1840

polymer

Transport properties of hyperbranched and dendrimer-like star polymers

M.S. Hedenqvist[a,1], H. Yousefi[a], E. Malmström[a], M. Johansson[a], A. Hult[a], U.W. Gedde[a,*], M. Trollsås[b], J.L. Hedrick[b]

[a]*Department of Polymer Technology, Royal Institute of Technology, S-100 44 Stockholm, Sweden*
[b]*IBM Almaden Research Center, 650 Harry Road, San José, CA 95120-6099, USA*

Received 5 October 1998; received in revised form 11 March 1999; accepted 5 May 1999

Abstract

Moisture transport properties were assessed by sorption and desorption measurements on hydroxyl-functional hyperbranched polyesters based on 2,2-bis(methylol) propionic acid (bis-MPA) as AB_2-monomer with ethoxylated pentaerythritol. A series of these polymers with different molar masses were studied. For the first time, it is reported that sigmoidal sorption curves were successfully modelled using a time-dependent surface boundary concentration, where the relaxation time was obtained from the mechanical stress relaxation data. The zero concentration diffusivities were very small and comparable with the values of fully amorphous poly(vinyl alcohol). Both the diffusivity data and the stress relaxation data indicated that these materials were plasticized by moisture. Ethylene glycol transport properties were measured on a hexadecanoate(C16)-terminated bis-MPA hyperbranched polymer. The replacement of the hydroxyl groups with C16 paraffin tails resulted in an increase in solute diffusivity despite the fact that these polymers became semicrystalline. The shape of the desorption curves indicated that continuous micropores were present and facilitated mass transport. The moisture transport properties were also measured on a series of semicrystalline dendrimer-like star poly(ε-caprolactone(s)). The low measured densities of these highly crystalline dendrimers confirmed that the porosity, as indicated by the shape of the desorption curves, had to be discontinuous. The porosity in the (C16)-terminated and the poly(ε-caprolactone(s)) was impossible to eliminate by applying a high external pressure during crystallization. A collective view of all the results obtained confirm that the transport properties are primarily controlled by the hydroxyl group concentration.

Keywords: Diffusivity; Solubility; Moisture

1. Introduction

The solubility and diffusivity properties of hyperbranched and dendritic polymers are significant in the perspective of their use in applications such as encapsulating components in drug delivery systems or food applications and as components in active packagings [1–6]. A hyperbranched polymer having a crystalline surface may, for example, be doped with aroma compounds and subsequently blended with coffee or tea or placed in the tea bag material. Upon heating the coffee or tea, the crystalline surface layer will melt and the aroma compounds will be released at the time of drinking. Alternatively, the hyperbranched polymer may migrate from the package to the foodstuff in a controlled way and subsequently release the aroma compounds when it reaches the foodstuff. All these features are dependent upon the transport properties of these materials. To our knowledge, no papers have been published concerning the transport properties of hyperbranched polymers. This paper presents diffusivity data relating to small molecules in a range of amorphous and semicrystalline hyperbranched polymers. The influence of the molecular architecture was assessed by comparing diffusivity data of the hyperbranched polymers with that of their linear analogues. Malmström et al. [7] showed that hyperbranched polymers form a globular morphology in some cases with a highly crystalline shell structure, which indeed is clearly different from the morphology of their linear counterparts.

The calculation of diffusivity from sorption data is complex in the instance of highly swollen systems because of the swelling-induced stresses that interfere with solute diffusion and lead to time-dependent surface boundary solute concentrations [8]. If, however, the surface concentration relaxation time (τ) describing the time dependence of the surface concentration could be obtained from another independent experiment such as a mechanical stress relaxation experiment, the

* Corresponding author. Tel.: +46-8-790-7640; fax: +46-8-790-6946.
E-mail address: gedde@polymer.kth.se (U.W. Gedde)
[1] Also at Packforsk-Swedish Packaging Research Institute, P.O. Box 9, S-164 93 Kista, Sweden.

0032-3861/00/$ - see front matter
PII: S0032-3861(99)00336-5

Nomenclature

T_m^0	equilibrium melting temperature
α_D	constant describing the magnitude of concentration dependence of D
Δh_f^0	heat of fusion for 100% crystalline polymer
$\tau_i(C)$	concentration-dependent stress relaxation time of Maxwell element i
α_{i_σ}	constant describing the magnitude of concentration dependence of s_i
α_{i_τ}	constant describing the magnitude of concentration dependence of t_i
C, C_1	solute concentration
C_0, C_∞	initial and equilibrium solute concentrations
D	diffusion coefficient
DB	degree of branching
D_{co}	diffusion coefficient at zero solute concentration
D_{coa}	diffusion coefficient at zero solute concentration of the amorphous component
DP	degree of polymerization
E(t)	time-dependent Young's modulus
E_{ico}	Young's modulus at zero solute concentration of Maxwell element i
F_0	rate of evaporation
$H(t)$	relaxation time distribution
h	step length along the spatial direction
i	integral number of the spatial position slong x
j	integral number of the spatial position along y
k	integral number of the spatial position along z
K_τ	term describing the time dependence of the boundary concentration
l	plate thickness
L	thickness of half the plate or half the slab
L_c	crystal thickness
m	integral number of the time position
N	number of space points along one cartesian direction in the slab
n	number of x-coordinates
r	sphere radius
R	the gas constant
ρ_1	solute density
ρ_2	polymer density
σ	solute-induced mechanical stress
$S_{1,1a}$	solubility of solute in the whole sample (1) and in the amorphous polymer component (1a)
σ_ε	crystal fold surface free energy
$\sigma_i(C)$	concentration-dependent stress of Maxwell element i
σ_{ico}	stress at zero solute concentration of Maxwell element i
$\sigma_\Sigma(C)$	the sum of the stress terms of each Maxwell element i
T	temperature
t	time
τ_{ico}	surface relaxation time at zero solute concentration of Maxwell element i
T_m	melting temperature
$v_{1,2}$	volume fractions of solute (1) and polymer (2), respectively
$v_{1a,2a}$	volume fractions of solute (1) and polymer (2), respectively confined to the amorphous parts
$w_{1,2}$	mass fractions of solute (1) and polymer (2), respectively
x	space coordinate

calculation of diffusivity from sorption data would be greatly facilitated [9]. In this paper, τ in moisture/hyperbranched polymer systems is determined from stress relaxation measurements and is used in the diffusion equations fitted to experimental sorption data.

2. Experimental

2.1. Materials

The water used was purified by ion exchange and

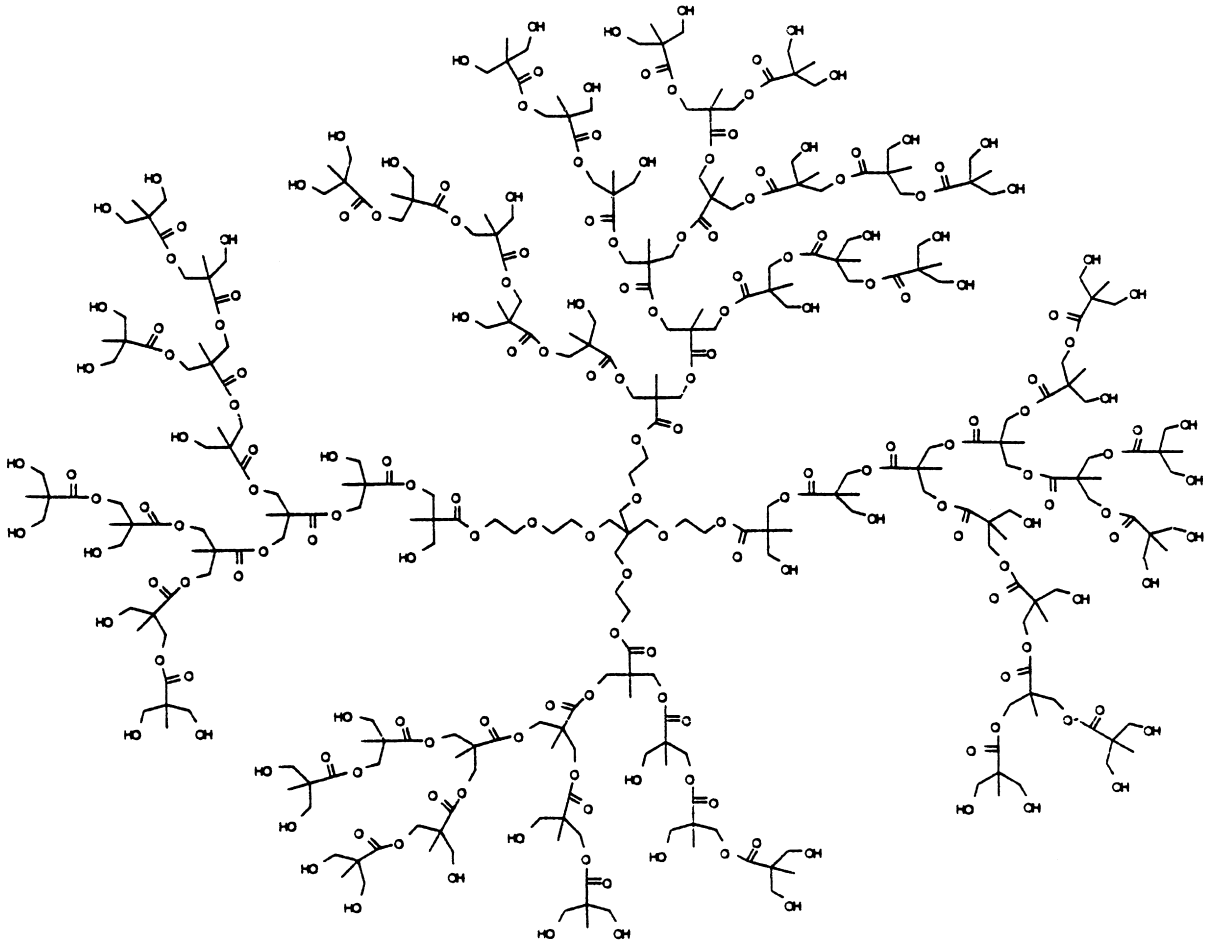

Fig. 1. Structure of HH4.

distillation (density $\rho_1 = 997$ kg m^{-3} (297.2 K)). The ethylene glycol was a 99.5% purity grade (Kebo Lab., Sweden; $\rho_1 = 1110$ kg m^{-3}).

Hydroxyl-functional hyperbranched polymers (denoted HHx, where *x* is the number of generations in the polymer) based on ethoxylated pentaerytritol (PP50, Perstorp) as core molecule and various amounts of 2,2-bis(methylol) propionic acid (bis-MPA) as AB_2-monomers were used (Fig. 1). The HHx materials were obtained from Perstorp Polyols, Perstorp AB, Sweden. Hexadecanoate(C16)-terminated bis-MPA/PP50 hyperbranched polymers denoted CAx (*x* refers to the number of generations) were also studied. Further details about the synthesis of these polymers are given by Malmström et al. [7]. The synthesis of the dendrimer-like star poly(ε-caprolactone(s)), denoted PCLx, where *x* is the number of generations, is described by Trollsås and Hedrick [10]. The core molecule was a bis-MPA derivative containing six hydroxyl groups and all generations were hydroxyl-functionalized (Fig. 2). Linear poly(ε-caprolactone) (Tone P747, Union Carbide), denoted LPCL, was also studied. Further details about the molecular structure of the studied polymers are given in Table 1.

Films of HHx were obtained by compression moulding at 373–393 K for 2 min without pressure followed by 5 min at 15 MPa and cooling in air (~10 K min^{-1}) using a Schwabenthan compression moulding machine (Polystat 400s). Spherical or cubical samples were cut from compression moulded specimens [moulding temperature: 340 K using very low pressure (<1 MPa) and cooled in air (~10 K min^{-1})] of CAx and PCLx.

2.2. Sorption and desorption measurements

The sorption experiment was carried out by storing originally dried HHx films (40×40 mm^2 with a thickness of 0.45–0.5 mm) in a desiccator at 14% relative humidity at 297.2 K. The weight increase was recorded by intermittently weighing the samples using a Mettler–Toledo AG245 balance. After reaching sorption equilibrium, the samples were transferred to another desiccator at 0% relative humidity at 297.2 K using silica pentoxide as drying substance and the desorption process was monitored by intermittent weighing.

Desorption measurements were performed on solute-saturated CAx, PCLx and LPCL at 297.2 K using a Mettler–Toledo TGA-SDTA 851 thermogravimetric

Table 1
Characteristics of samples

Sample	Generation[a]	Structure[b]	M[c]	DB[d]	Density[e]
HH3[f]	3	28[j]	3600	42	1.299
HH4[f]	4	60[j]	7300	42	1.301
HH6[f]	6	252[j]	29 580	42	1.3105
CA2[g]	2	12[j]	5560	42	1.055
CA4[g]	4	60[j]	22 580	42	1.070
CA6[g]	6	252[j]	90 650	42	1.017
PCL1[h]	1	6[k]	14 300	100	0.995–1.040
PCL2[h]	2	18[k]	42 300	100	0.994–1.125
PCL3[h]	3	42[k]	96 000	100	0.991–1.126
LPCL[i]	–	–	40 000	0	1.140

[a] Defined as the number of theoretical layers.
[b] Branch units/core units.
[c] Calculated molar mass based on stoichiometry (g mol^{-1}).
[d] Degree of branching (%).
[e] Determined using Archimedes principle (g cm^{-3}), the lower and the higher density values of PCL samples are from measurements on spheres and slabs respectively.
[f] Hyperbranched hydroxyl-terminated aliphatic polyesters based on bis(methylol) propionic acid (bis-MPA) as AB_2 monomers with ethoxylated pentaerythritol (PP50) as core molecule.
[j] Number of bis-MPA per core molecule (PP50).
[g] Hyperbranched alkyl(C16)-terminated bis-MPA/PP50.
[h] Dendrimer-like star poly(ε-caprolactone).
[k] Number of ε-caprolactone units per core molecule (bis-MPA derivative).
[i] Linear poly(ε-caprolactone).

instrument. Due to the small amount of material available, the specimens were either shaped as spheres with a diameter of 6–7 mm or as cubes with 3–5 mm sides. Prior to desorption, the CAx samples were sorbed to equilibrium in liquid ethylene glycol at 297.2 K and the PCLx and LPCL samples were sorbed to equilibrium moisture uptake by putting them in a desiccator at 100% relative humidity at 297.2 K.

2.3. Oxygen permeability measurements

The permeability of oxygen through HHx at 298.2 K was obtained using a Mocon OX-TRAN TWIN device which uses a coulometric sensor to detect oxygen. Degassed film samples with a thickness of 0.45–0.5 mm were mounted in an isolated diffusion cell and were subsequently surrounded by flowing nitrogen gas to remove sorbed oxygen from the samples. The sample had a circular exposure area of 5×10^{-4} m^2 achieved by covering a part of the film with a tight aluminium foil. One side of the sample was initially exposed to flowing oxygen containing 1% hydrogen at atmospheric pressure. The oxygen concentration was zero on the other side. The flow rate (Q) through the sample was measured and, from the steady-state flow rate (Q_∞), the oxygen permeability coefficient (P) was calculated.

2.4. Stress relaxation

Stress relaxation was measured on 65 mm long dumb-bell shaped specimens (thickness: 0.45–0.5 mm; width of narrow section: 5 mm; gauge length: 22 mm) rapidly strained to 5% engineering strain, with a ramp time less than 1 s, at 297.2 K and 50% relative humidity using an Instron Testing Instrument Model 5566 equipped with a video camera recording the strain optically. Before the stress relaxation measurement, the samples tested were exposed to 100% relative humidity for different times. The loss or gain of moisture during the stress relaxation tests (testing time: ≈40 min) was insignificant.

2.5. Density measurements

The densities (ρ_2) at 296.2 K of the samples were determined by weighing in air and in water and applying the Archimedes principle.

2.6. Differential scanning calorimetry

The melting endotherms of the polymers were obtained by heating 5 ± 1 mg samples at a rate of 10 K min^{-1} using a temperature- and energy-calibrated Mettler–Toledo DSC 820.

3. Theory

3.1. Sorption/desorption kinetics of film samples

For a plate geometry (Fig. 3), Fick's second law of diffusion [11]:

$$\frac{\partial C}{\partial t} = \frac{\partial}{\partial x}\left(D(C)\frac{\partial C}{\partial x}\right) \tag{1}$$

is solved where C is the penetrant concentration given in g cm^{-3}. Only half the plate thickness is considered and the inner boundary coordinate is described as an isolated point:

$$\left(\frac{\partial C}{\partial x}\right)_{x=L} = 0. \tag{2}$$

The outer boundary condition is described by:

$$\left[\tau\frac{\partial C}{\partial t}\right]_{x=0} + (C - C_\infty)_{x=0} = 0 \tag{3}$$

where C_∞ is the final concentration calculated as:

$$C_\infty = \frac{w_1\rho_2}{1 + (w_1\rho_2/\rho_1)} \tag{4}$$

and τ is the surface concentration relaxation time, w_1 is the solute equilibrium mass concentration given in kg (kg polymer)$^{-1}$, and C_0 is the initial boundary concentration. During desorption, evaporation takes place at the surface, and is described by the following equation:

$$D(C)\left[\frac{\partial C}{\partial x}\right]_{x=0} = F_0 C \tag{5}$$

where F_0 is the evaporation constant (cm s^{-1}) calculated to be $3 \times 10^{-5} - 3 \times 10^{-6}$ for the systems concerned [12]. The

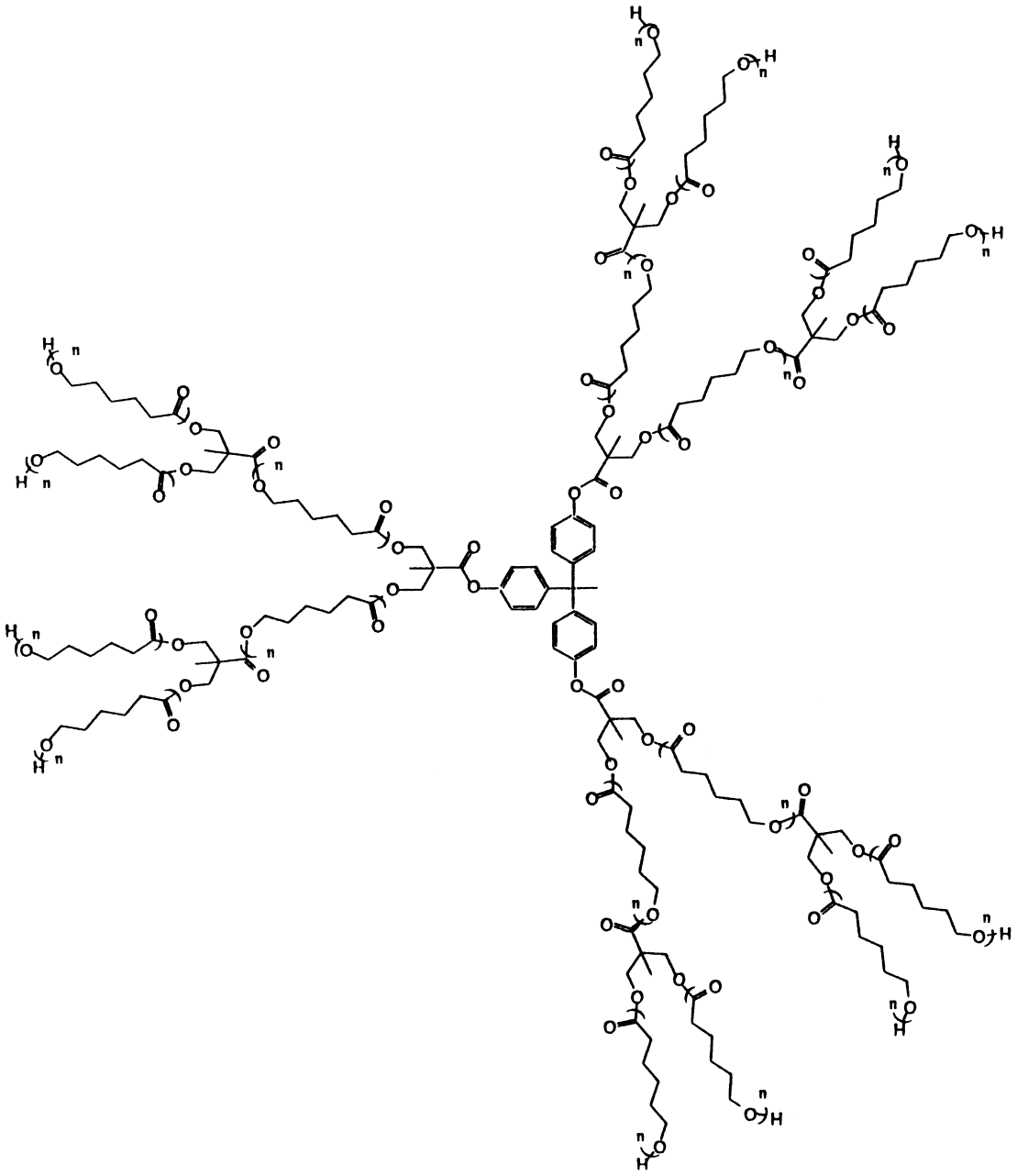

Fig. 2. Structure of PCL2.

concentration-dependent diffusivity ($D(C)$) is expressed as [11]:

$$D(C) = D_{co} e^{\alpha_D C} \quad (6)$$

where D_{co} is the zero concentration diffusivity and α_D is a constant. This equation has been used extensively and shown that it fits diffusivity data well [8,9]. Additionally, it can be derived and motivated by applying free volume theories [8,13]. It should be pointed out, however, that a linear relationship could fit the concentration dependent diffusivity as well as Eq. (6), as reported by Hedenqvist

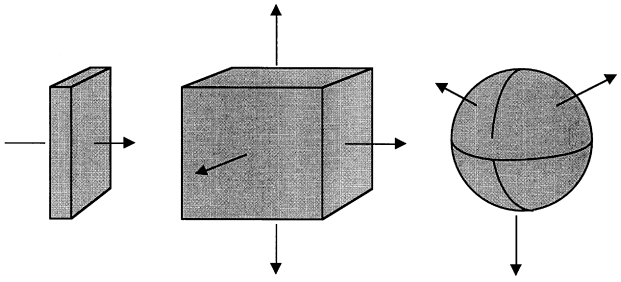

Fig. 3. Plate, slab and sphere geometries. Arrows indicate flow of solute.

and Gedde [9]. By inserting Eq. (6) in Eq. (1) and discretizing, the following expression is obtained:

$$\frac{\partial C}{\partial t} = f(t,C) = \frac{D_{co}}{\Delta x_i^2}(e^{\alpha_D C_{i+0.5}}(C_{i+1} - C_i) - e^{\alpha_D C_{i-0.5}}(C_i - C_{i-1})) \quad (7)$$

where

$$C_{i\pm 0.5} = \frac{C_i + C_{i\pm 1}}{2}. \quad (8)$$

Eq. (2) is best discretized using

$$C_{n+1} = C_{n-1}. \quad (9)$$

Note that $i = n$ at the centre of the plate. The surface boundary condition ($i = 0$), given by Eq. (5), may be written explicitly as:

$$C_0 = \frac{C_1}{1 + (\Delta x_i F_0 / D_{co} e^{\alpha_D C_1})}. \quad (10)$$

The concentration profiles were generated using the following implicit multi-step relationship (m is the time coordinate):

$$\nabla^3 C_{m+1} = \frac{6}{11}\Delta t_m \left(f(t_{m+1}, \nabla^3 C_{m+1} + \nabla^2 C_m + \nabla C_m + C_m) - \frac{1}{\Delta t_m}\left(\frac{3}{2}\nabla^2 C_m + \nabla C_m\right)\right). \quad (11)$$

The details of the method are described by Hedenqvist et al. [14]. The implicit method integrates with respect to time using arcs with three constant time steps but with a variable step-size between them. The first arc is produced by a three-stage second-order Runge–Kutta method [15]. The concentration profiles were integrated using Simpson's method with the Romberg routine to obtain higher accuracy.

3.2. Desorption kinetics for slab (Fig. 3):

For a slab, Fick's second law of diffusion [11]:

$$\frac{\partial C}{\partial t} = \frac{\partial}{\partial x}\left(D(C)\frac{\partial C}{\partial x}\right) + \frac{\partial}{\partial y}\left(D(C)\frac{\partial C}{\partial y}\right) + \frac{\partial}{\partial z}\left(D(C)\frac{\partial C}{\partial z}\right) \quad (12)$$

is solved and discretized according to:

$$\frac{\partial C}{\partial t} = f(t,C) = \frac{D_{co}}{\Delta x_i^2}(e^{\alpha_D C_{i+0.5,j,k}}(C_{i+1,j,k} - C_{i,j,k}) - e^{\alpha_D C_{i-0.5,j,k}}(C_{i,j,k} - C_{i-1,j,k})) \quad (13)$$

which at each time step is integrated over i, j and k (associated with the x, y and z directions, respectively). The Jacobian matrix needed for the multi-step method is calculated using the relationships (Eqs. (14)):

$$\frac{\partial f(t,C)}{\partial C_{i-1}} = \frac{D_{co}}{\Delta x_i^2}\left(e^{\alpha_D C_{i-0.5,j,k}} - \frac{\alpha_D}{2}e^{\alpha_D C_{i-0.5,j,k}}(C_{i,j,k} - C_{i-1,j,k})\right) \quad (14)$$

$$\frac{\partial f(t,C)}{\partial C_i} = \left[\frac{\partial f(t,C)}{\partial C_i}\right]_x + \left[\frac{\partial f(t,C)}{\partial C_i}\right]_y + \left[\frac{\partial f(t,C)}{\partial C_i}\right]_z \quad (15)$$

which may be written as:

$$\begin{aligned}\frac{\partial f(t,C)}{\partial C_i} = \frac{D_{co}}{\Delta x_i^2}\Bigg(& \frac{\alpha_D}{2}e^{\alpha_D C_{i+0.5,j,k}}(C_{i+1,j,k} - C_{i,j,k}) - e^{\alpha_D C_{i+0.5,j,k}} \\ & - \frac{\alpha_D}{2}e^{\alpha_D C_{i-0.5,j,k}}(C_{i,j,k} - C_{i-1,j,k}) - e^{\alpha_D C_{i-0.5,j,k}}\Bigg) \\ & + \frac{\alpha_D D_{co}}{\Delta y_i^2}(e^{\alpha_D C_{i,j+0.5,k}}(C_{i,j+1,k} - C_{i,j,k}) \\ & - e^{\alpha_D C_{i,j-0.5,k}}(C_{i,j,k} - C_{i,j-1,k})) \\ & + \frac{\alpha_D D_{co}}{\Delta z_i^2}(e^{\alpha_D C_{i,j,k+0.5}}(C_{i,j,k+1} - C_{i,j,k}) \\ & - e^{\alpha_D C_{i,j,k-0.5}}(C_{i,j,k} - C_{i,j,k-1}))\end{aligned} \quad (16)$$

$$\frac{\partial f(t,C)}{\partial C_{i+1}} = \frac{D_{co}}{\Delta x_i^2}\left(\frac{\alpha_D}{2}e^{\alpha_D C_{i+0.5,j,k}}(C_{i+1,j,k} - C_{i,j,k}) + e^{\alpha_D C_{i+0.5,j,k}}\right). \quad (17)$$

The solution to the case of a slab is integrated in time using the multi-step method.

3.3. Desorption kinetics for spherical geometry (Fig. 3)

For a sphere (r = radius), Fick's second law of diffusion [11]:

$$\frac{\partial C}{\partial t} = \frac{\partial}{\partial r}\left(D(C)\frac{\partial C}{\partial r}\right) + \frac{2}{r}\left(D(C)\frac{\partial C}{\partial r}\right) \quad (18)$$

is solved and discretized according to:

$$\begin{aligned}\frac{\partial C}{\partial t} = f(t,C) = & \frac{D_{co}}{\Delta r_i^2}(e^{\alpha_D C_{i+0.5}}(C_{i+1} - C_i) - e^{\alpha_D C_{i-0.5}}(C_i - C_{i-1})) \\ & + \frac{2D_{co}}{\Delta r_i}\left(\frac{e^{\alpha_D C_{i+0.5}}}{r_{i+0.5}}(C_{i+1} - C_i) - \frac{e^{\alpha_D C_{i-0.5}}}{r_{i-0.5}}(C_i - C_{i-1})\right).\end{aligned} \quad (19)$$

The Jacobian matrix is calculated using the relationships

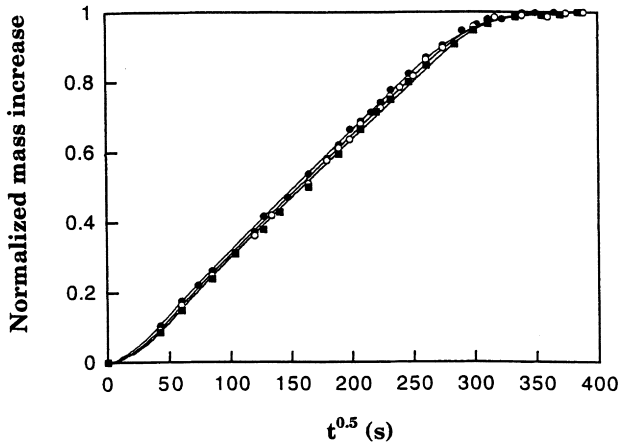

Fig. 4. Normalized mass increase (moisture sorption) as a function of time for HH3 (●), HH4 (○) and HH6 (□). Solid lines are best fits using Eqs. (1)–(3), (6)–(9), (11) and (25)–(27).

(Eqs. (20)–(22)):

$$\frac{\partial f(t,C)}{\partial C_{i-1}} = \frac{D_{co}}{\Delta r^2}\left(e^{\alpha_D C_{i-0.5}} - \frac{\alpha_D}{2}e^{\alpha_D C_{i-0.5}}(C_i - C_{i-1})\right) + \frac{2D_{co}}{r_{i-0.5}\Delta r}\left(e^{\alpha_D C_{i-0.5}} - \frac{\alpha_D}{2}e^{\alpha_D C_{i-0.5}}(C_i - C_{i-1})\right) \quad (20)$$

$$\frac{\partial f(t,C)}{\partial C_i} = \frac{D_{co}}{\Delta r^2}\left(\frac{\alpha_D}{2}e^{\alpha_D C_{i+0.5}}(C_{i+1,} - C_i) - e^{\alpha_D C_{i+0.5}} - \frac{\alpha_D}{2}e^{\alpha_D C_{i-0.5}}(C_{i,} - C_{i-1}) - e^{\alpha_D C_{i-0.5}}\right) + \frac{2}{\Delta r^2}\left(\frac{\alpha_D D_{co}}{r_{i+0.5}}e^{\alpha_D C_{i+0.5}}(C_{i+1} - C_i) - \frac{e^{\alpha_D C_{i+0.5}}}{r_{i+0.5}} - \frac{\alpha_D D_{co}}{r_{i-0.5}}e^{\alpha_D C_{i-0.5}}(C_i - C_{i-1}) - \frac{e^{\alpha_D C_{i-0.5}}}{r_{i-0.5}}\right) \quad (21)$$

$$\frac{\partial f(t,C)}{\partial C_{i+1}} = \frac{D_{co}}{\Delta r^2}\left(\frac{\alpha_D}{2}e^{\alpha_D C_{i+0.5}}(C_{i+1,} - C_i) + e^{\alpha_D C_{i+0.5}}\right) + \frac{2D_{co}}{r_{i+0.5}\Delta r}\left(e^{\alpha_D C_{i+0.5}} + \frac{\alpha_{De}}{2}e^{\alpha_D C_{i+0.5}}(C_{i+1} - C_i)\right). \quad (22)$$

The solution is integrated with respect to time using the multi-step method (Eq. (11)).

4. Results and discussion

Fig. 4 shows the moisture sorption curves of the three HHx materials. The s-shape of the sorption curves is evident and it indicates that the boundary concentration is time-dependent, as described by the relaxation time (τ) in Eq. (2). The saturation moisture content at 14% relative humidity was 0.044–0.05 g cm^{-3} (Table 2) and it is well known that such an extensive solute uptake leads to a time-dependence of the boundary concentration [9]. A low relative humidity was chosen because of the moisture sensitivity of the samples.

Table 2
Parameters in Eqs. (25) and (26) used to fit HH3 sorption and desorption curves

Parameter[a]	Samples		
	HH3	HH4	HH6
D_{co} (cm^2 s^{-1})	3.0×10^{-10}	1.0×10^{-10}	0.5×10^{-10}
α_D (cm^3 g^{-1})	66	106	140
C_0[b]	0.25	0.25	0.25
τ_{1co} (h)	20.1	–	–
α_{1t} (cm^3 g^{-1})	9.53	–	–
τ_{2co} (h)	1.46	–	–
α_{2t} (cm^3 g^{-1})	1.23	–	–
τ_{3co} (h)	0.50	–	
α_{3t} (cm^3 g^{-1})	1.95	–	–
σ_{1co} (MPa)	0.06	–	–
α_{1s} (cm^3 g^{-1})	−2.77	–	–
σ_{2co} (MPa)	0.195	–	–
α_{2s} (cm^3 g^{-1})	7.00	–	–
σ_{3co} (Mpa)	0.30	–	–
α_{3s} (cm^3 g^{-1})	10.4	–	–
D_{co} (cm^2 s^{-1})[c]	4.0×10^{-10}	2.8×10^{-10}	2.5×10^{-10}
α_D (cm^3 g^{-1})[c]	45	56	62
S_1 (g cm^{-3})[d]	0.053	0.044	0.045

[a] Obtained from data of sorption experiments or stress relaxation measurements.
[b] Normalized solute concentration.
[c] Data from desorption experiments.
[d] Moisture solubility in gram solute per cm^3 polymer at 14% relative humidity.

The boundary concentration relaxation time (τ) is normally treated as an adjustable parameter determined by

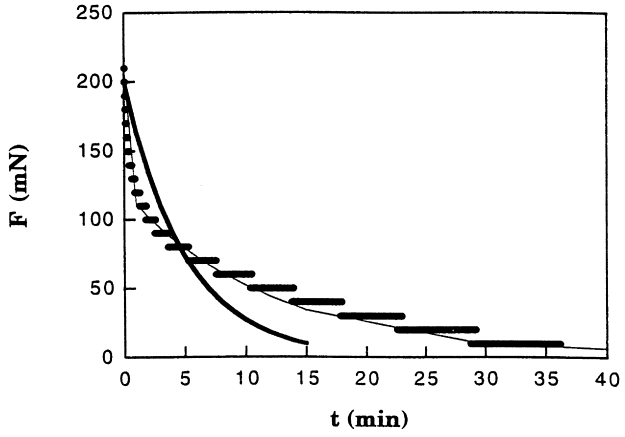

Fig. 5. Stress relaxation of HH3 conditioned in air at 50% relative humidity. The thin and the thick lines represent the best fits using a three-Maxwell-element model and a single Maxwell element, respectively.

fitting the equations to the sorption data. It is believed that the non-uniform concentration of solute during the uptake period induces mechanical stresses in the specimens which counteract sorption. Here, we attempt another approach, namely to use the mechanical relaxation data to assess the relaxation time spectrum and to use the data in the sorption kinetics equations. The stress relaxation data of specimens strained to 5% were fitted to the Maxwell model. Although the strains due to the moisture sorption were not equal to 5%, the stress relaxation data taken at 5% strain were used because the stress relaxation times are reported to be independent of strain within limited strain regions [16,17]. Only one Maxwell term was clearly inadequate in describing the experimental data. Three parallel-coupled Maxwell elements (Eq. (23)) were required to fit the experimental stress relaxation data (Fig. 5).

$$\sigma(t, C) = \sum_{i=1}^{3} \sigma_i(C) \mathrm{e}^{-\frac{t}{\tau_i(C)}}. \tag{23}$$

Fig. 6 shows the relaxation time spectrum [$H(t)$] of HH3 defined as:

$$H(t) = -\frac{\partial E(t)}{\partial \ln(t)}. \tag{24}$$

In this figure, $H(t)$ is however calculated from the fitted three-component Maxwell model and not from the experimental data. The peak is located at $t \approx 7.5$ min and the distribution is skewed.

Eq. (23) was fitted to the stress relaxation data of specimens containing different amounts of moisture and this enabled the three stress relaxation times (Fig. 7), and thus the stresses to be calculated as a function of moisture content (Table 2):

$$\tau_i(C) = \tau_{i\mathrm{co}} \mathrm{e}^{-\alpha_{i\tau} C} \tag{25}$$

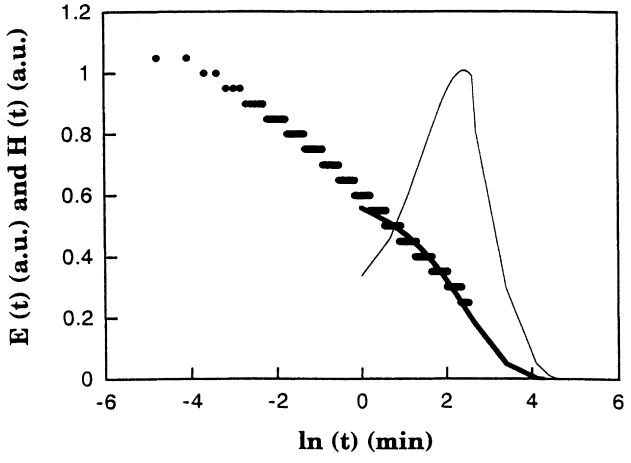

Fig. 6. Normalized Young's modulus of HH3 conditioned in air at 50% relative humidity as a function of time. The thick line is the best fit using the three Maxwell elements. The thin line corresponds to the relaxation time distribution ($H(t)$).

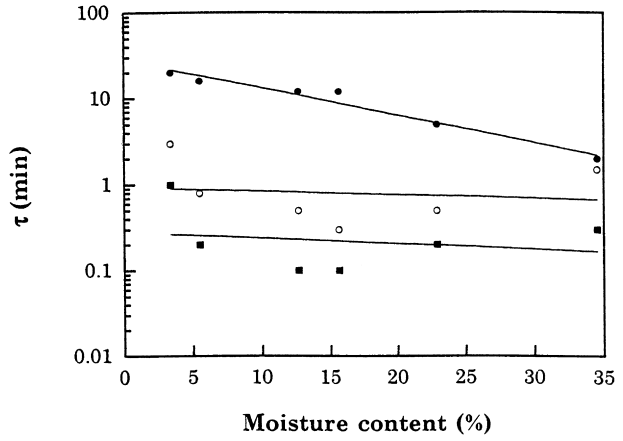

Fig. 7. Stress relaxation times corresponding to the three parallel-coupled Maxwell elements (Eq. (23)) as a function of volume fraction of moisture for HH3: τ_1 (●); τ_2 (○);and τ_3 (□).

$$\sigma_i(C) = \sigma_{i\mathrm{co}} \mathrm{e}^{-\alpha_{i\sigma} C} \tag{26}$$

where $\alpha_{i\tau}$ and $\alpha_{i\sigma}$ are constants and $\tau_{i\mathrm{co}}$ and $\sigma_{i\mathrm{co}}$ are the zero concentration relaxation time and zero concentration stress of the Maxwell element i. It is seen in Fig. 7 that at least the longest relaxation time (τ_1) follows Eq. (25). Due to the approximate nature of Eq. (23), the fit of the mechanical relaxation data at short times was associated with some error, which in turn resulted in scattering in the calculated shorter relaxation times (τ_2 and τ_3). Nisizawa [18] used a single-component Maxwell model to describe stress relaxation in polyethylene swollen in a series of different solvents. In Table 2, the fitted parameters to Eqs. (23), (25) and (26) are presented. The calculated relaxation time spectrum obtained for HH3 was used to describe the boundary condition (Eq. (3)) which may be rewritten as:

$$C = C_0 + (C_\infty - C_0)(1 - K_\tau) \tag{27}$$

where

$$K_\tau = \sum_{i=1}^{3} \frac{\sigma_i(C)}{\sigma_\Sigma(C)} \mathrm{e}^{-\frac{t}{\tau_i(C)}} \tag{28}$$

and $\sigma_\Sigma(C)$ is the sum of the three concentration stress terms ($\sigma_i(C)$) in Eq. (23), assuming that the stress decreases exponentially with increasing moisture content. Fig. 8 and Table 2 indeed show that both stress and Young's modulus decrease exponentially with increasing moisture content. As shown in Fig. 4, the fit of Eqs. (1)–(3), (6)–(9), (11) to the experimental sorption data is excellent for all HHx samples using the stress relaxation time data obtained for HH3. Thus, there seems to be a close resemblance between stress relaxation and relaxation of the boundary solute concentration, both given by the same τ distribution. The applicability of the stress relaxation time data of HH3 data to all HHx materials indicates that the stress relaxation behaviour is similar for the HHx samples studied.

Fig. 9 shows that the time exposure to moisture is

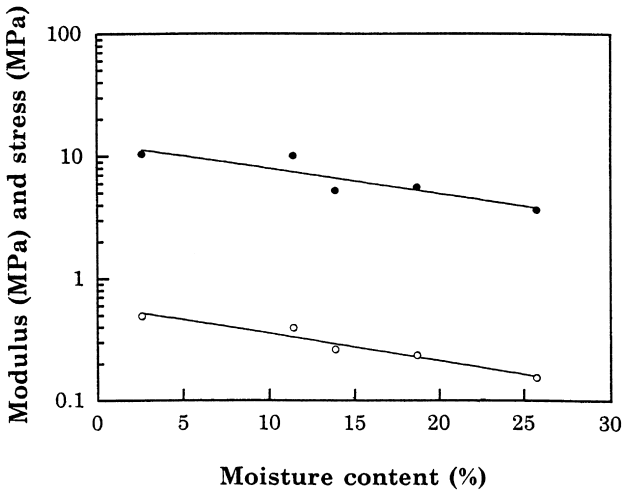

Fig. 8. Young's modulus (●) and initial stress at 5% strain (○) as a function of the volume fraction of moisture for HH3.

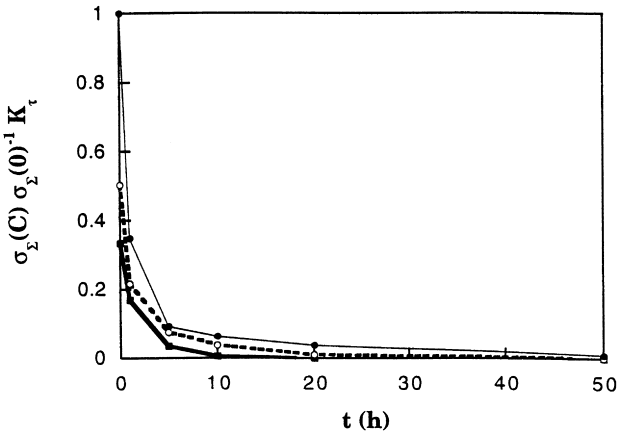

Fig. 10. Normalized stress calculated from Eq. (28) at different moisture contents given in g water cm^{-3} polymer: (●) $C = 0$; (○) $C = 0.10$; and (□) $C = 0.20$.

important for the stress–strain behaviour of the samples. The moisture-concentration-dependence of the stress shows a considerable dependence on exposure time. These so-called "time effects" have also been observed in other systems and it has been suggested that they are due to slow relaxation of constrained chain segments [8]. From the data presented in Fig. 10, the time to reach the equilibrium surface concentration can be estimated. Depending on the solute concentration, the equilibration time range between 10 and more than 50 h, the longest equilibration time being obtained for the dry sample. In Fig. 11, the fitted desorption curves of the HHx samples are shown. The fitted parameters presented in Table 2 confirm that the diffusion coefficient is solute-concentration-dependent. The α_D and D_{co} values obtained from the sorption data were higher than those calculated from desorption data; a finding which again demonstrates the importance of "time effects". The oxygen permeability data presented in Table 3 show that the permeability increased with moisture content but, in contrast to the mechanical and the moisture diffusion data, seems to be rather insensitive to the moisture exposure time.

Fig. 12 shows the solubility of moisture as a function of hydroxyl concentration in the HHx polymers. The hydroxyl concentration is calculated according to:

$$C_{OH} = 2^{n_g+2}\frac{\rho_2}{M_2} \tag{29}$$

assuming that no backbiting reaction takes place. Calculations based on Eq. (29) show that there is a very small (≈1.5%) decrease in hydroxyl concentration with increasing molar mass, i.e. with increasing number of generations per molecule, primarily because the density decreased with increasing molar mass (Table 1). Ester groups are obviously also present in these polymers, and they also attract water molecules. The concentration of ester groups increases with increasing molar mass; by 11% going from generation 3 to

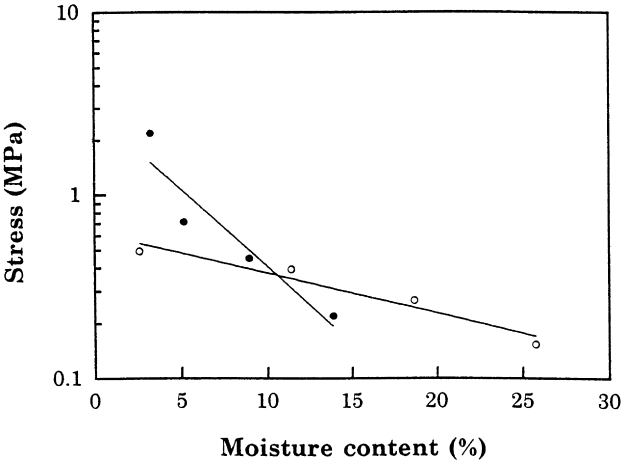

Fig. 9. Initial stress at 5% strain as a function of the volume fraction of moisture for HH3 samples saturated in moisture (100% relative humidity) for 3 days (●) and 50 days (○).

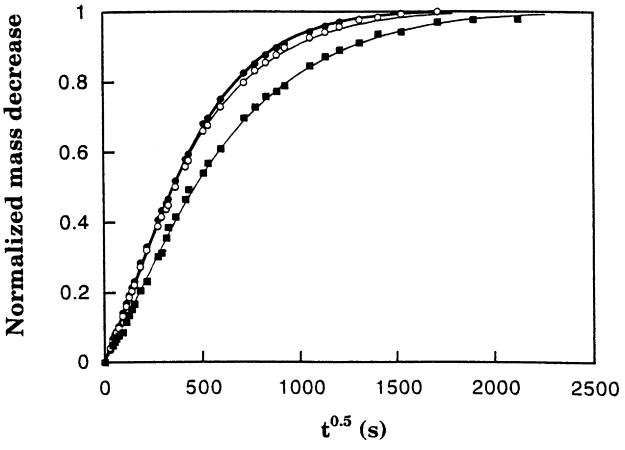

Fig. 11. Normalized mass decrease (moisture desorption) as a function of time for: HH3 (●); HH4 (○); and HH6 (□). Solid lines are best fits using Eqs. (1), (2) and (4)–(11).

Table 3
Oxygen permeability of HH3

Time after moulding[a] (h)	Humidity[b]	P[c]
538	0	0.55×10^{-10}
505	50	5.75×10^{-10}
16	50	7.08×10^{-10}

[a] Elapsed time from the moment of film making to the sampling of permeability data in the Mocon Instrument.
[b] Percentage relative humidity in the chamber of the Mocon Instrument.
[c] Permeability expressed in cm^3 (STP) cm cm^{-2} s^{-1} atm^{-1}.

generation 6. Fig. 12 shows that the moisture content increased with hydroxyl content. Note that the moisture content decreased with increasing ester group concentration, a finding that strongly indicate that the hydroxyl groups are strong water absorbants than the ester groups. This is consistent with data collected by van Krevelen [19] who found an order of magnitude difference in water absorbing capacity of the aforementioned groups. Calculations show that there are approximately 0.23–0.28 water molecules sorbed per hydroxyl group. This value is much lower than data obtained for other water–polymer pairs reported by van Krevelen [19], and this suggests that there is a fraction of the hydroxyl groups not readily available to the sorbed water molecules. There is also a decrease in polymer density with increasing hydroxyl concentration, which may partly explain the increase in moisture solubility and number of sorbed water molecules per hydroxyl group with increasing hydroxyl density (Fig. 12). Fig. 13 shows that D_{co} decreased markedly with increasing polymer density. The hydroxyl groups with their attractive forces acting on the water molecules should trap the water molecules and hence retard diffusion. However, the 1.5% increase in hydroxyl group content seems to be less significant than the stronger effect originating from density (free volume).

The average diffusivity on the other hand showed a more

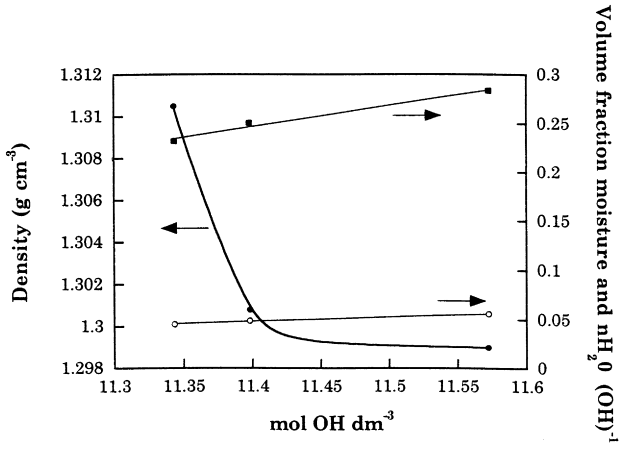

Fig. 12. Polymer (HHx) density (●), volume fraction of moisture (○) and number of water molecules sorbed per hydroxyl group (□) as a function of polymer hydroxyl concentration.

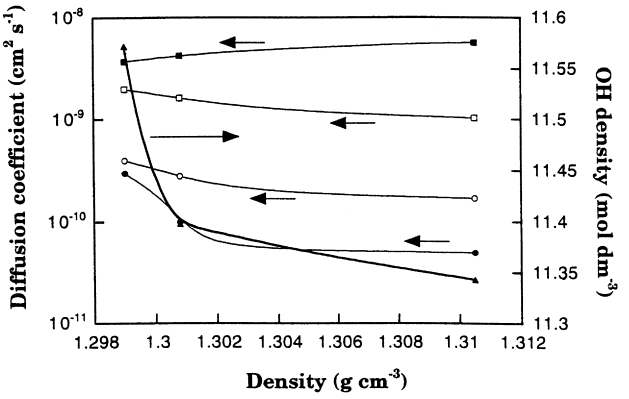

Fig. 13. Zero concentration diffusivity from sorption (●) and desorption (○) and average diffusivity from sorption (■) and desorption (□) and hydroxyl density (▲) as a function of density for HHx.

complex relationship with polymer density (Fig. 13). The presence of hydroxyl groups retarded moisture diffusivity due to strong secondary forces. Hence, it may be expected that, at the same time as a more dense structure leads to lower diffusivity, the decrease in hydroxyl content with increasing density acts in an opposite way thereby leading to a complex relationship between diffusivity and density. It seems that D_{co} is sensitive primarily to polymer density whereas the average diffusivity is a function of a combination of polymer and hydroxyl concentrations. The D_{co} values reported here show that penetrating species move very slowly in the unplasticized hyperbranched materials and that the diffusivities are lower or similar to that of amorphous poly(vinyl alcohol) [20]. Hence, as in other highly polar systems, it is the large amount of hydrogen bonds that limit the diffusivity of small molecules in these HHx-materials. It may finally be concluded that, although some trends may be observed, the changes in diffusivity and

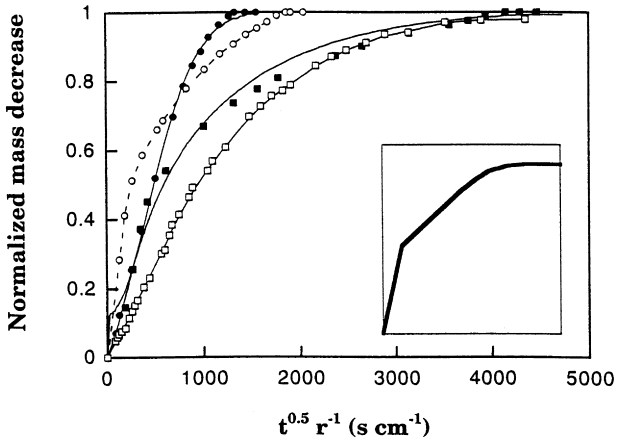

Fig. 14. Normalized mass decrease (ethylene glycol desorption) as a function of time for: CA4 slab (●); CA6 slab (○); CA4 sphere (■); and CA6 sphere (□). Solid lines are best fits using Eqs. (1), (2), (4)–(6), (10)–(22). The broken line is drawn along the CA6 slab data. The insert figure shows the schematic curve modelled using Eq. (26) in Ref. [21]. The axes of the insert figure have the same units as the larger figure.

Table 4
Ethylene glycol diffusivity and solubility data of CAx (obtained from desorption experiments)

Parameter	Sample		
	CA2	CA4	CA6
D_{co} ($cm^2\ s^{-1}$)[a]	–	9.0×10^{-8}	–
α_D ($cm^3\ g^{-1}$)[a]	–	2	–
D_{co} ($cm^2\ s^{-1}$)[b]	–	8.0×10^{-8}	7.0×10^{-8}
α_D ($cm^3\ g^{-1}$)[b]	–	8	5
S_1 ($g\ cm^{-3}$)[c]	0.009	0.018	0.010

[a] Obtained from CA-slabs.
[b] Obtained from CA-spheres.
[c] Ethylene glycol solubility in gram solute per cm^3 polymer; average values of slab and sphere samples.

physical properties with increasing number of generations for HHx are small.

Fig. 14 shows fitted ethylene glycol-desorption data of CA4 and CA6. Ethylene glycol diffusivities are similar for slab and sphere samples as well as for different generations (CA4 and CA6) (Table 4). The CA2 and CA6 slab-desorption curves showed two stages (Fig. 14) and reliable diffusivities could not be obtained. In Ref. [21], a similar desorption was modelled adding a pore-diffusion term to the Fickian equation. This is schematically shown in the insert figure of Fig. 14. It is thus suggested, on the basis of the shape of the desorption curves of the CAx materials, that these materials contained pore channels which are continuous (Fig. 15). CA4 did not show a two-stage desorption behaviour (Fig. 14). However, the greater diffusivity of this material compared with that of the hydroxyl-functional analogue suggests that pore diffusion also occurred in this material. The data presented in Table 4 show that the solubility was highest for the sample not showing the two-stage behaviour (CA4) and the solubility was also independent of

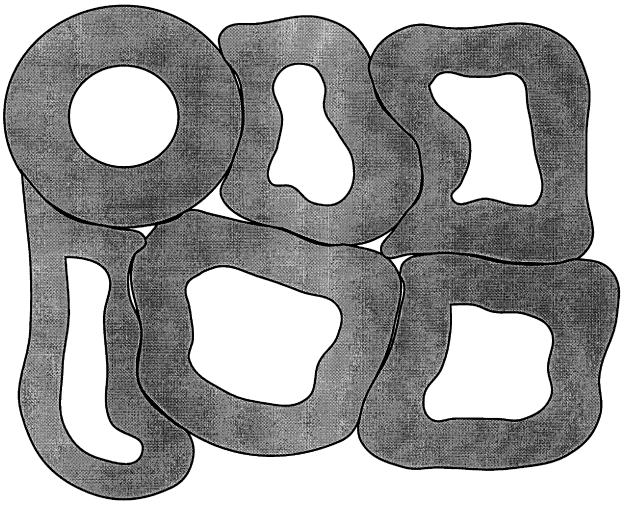

Fig. 15. Close packing of CAx molecules. Grey areas are C16 paraffin crystalline shells.

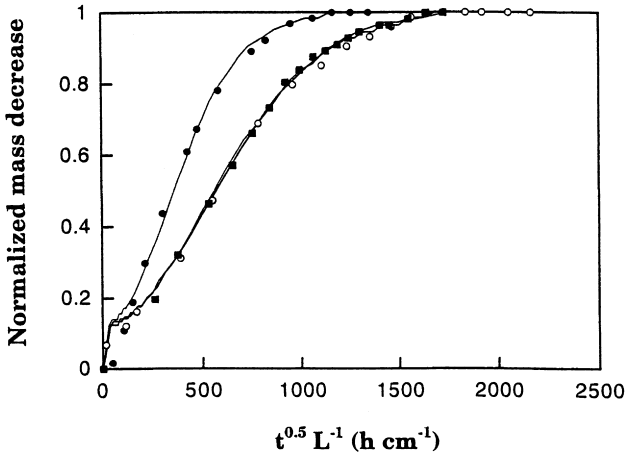

Fig. 16. Normalized mass decrease (moisture desorption) as a function of time for slabs of: PCL1 (●); PCL2 (○); and PCL3 (■). Solid lines are best fits using Eqs. (1)–(2), (4)–(6), (10)–(17).

the sample geometry, even though some samples showed the two-stage behaviour (CA2 and CA6). This suggests that pores exist even in the samples that do not show the two-stage desorption behaviour.

The morphology of CA4 was studied indirectly by treating it with chlorosulphonic acid at room temperature and then assessing and comparing the degradation rate with respect to that of a pure C22 paraffin. It was found that CA4 degraded much faster than C22. The slow degradation of the C22 paraffin is due to the almost complete absence of an amorphous component in this oligomer. A continuous crystalline shell on each hyperbranched polymer would give good protection for degradation of the internal, readily degradable material. The very rapid digestion of the CAx polymers suggests a discontinuous paraffin shell and possibly also the presence of pores.

The reason for the formation of pores (voids) in the CAx polymers can only be speculated upon. The crystallization of the paraffinic tail groups involves a volume decrease and it is not unlikely that the small stresses created by the volume change are sufficient to open up channels between the hydrophobic “grains” due to a weak interaction between different paraffinic layers (Fig. 15). Films of CA2 were prepared by compression moulding at high pressure to find out if CAx’s could be made pore-free. The densities of these films were however not higher than those of the slab and sphere samples, which indicated that pores did not disappear by applying high moulding pressures.

Fig. 16 presents experimental moisture desorption data of PCL1, PCL2 and PCL3 slabs together with best fits. Since, the computational work increased by a factor of N^3 when the number of spatial steps in each direction (N) increased, it was necessary to keep the spatial step size large and to use $N = 18$. This led to a large computational error and a large mismatch of the experimental data at the early stages of desorption (Fig. 16). It was shown, however, from the modelling of HHx-plates that the result of modelling

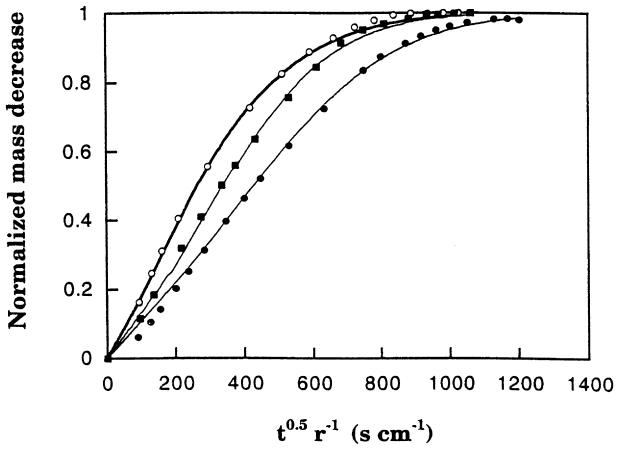

Fig. 17. Normalized mass decrease (moisture desorption) as a function of time for spheres of: PCL1 (●); PCL2 (○); and PCL3 (■). Solid lines are best fits using Eqs. (1)–(2), (4)–(6), (10), (11), (18)–(22).

using $N = 18$ at later stages basically overlapped with the result obtained by modelling using $N = 61$. Hence, the fit at later times, in the case of the slab, may be used to obtain proper diffusivity data. The moisture desorption data as well as best fits of the PCL spheres are given in Fig. 17. The fitted parameters for both slabs and spheres are given in Table 5, and interestingly they clearly show that the diffusivities and the solubilities are considerably larger for the dendritic polymers than for the linear analogue. The crystallinity of the LPCL sample was 52% according to density data using values for the crystalline and amorphous densities of: $\rho_c = 1187\ \mathrm{kg\ m^{-3}}$[22] and $\rho_a = 1094\ \mathrm{kg\ m^{-3}}$[22]. The crystallinities of the dendritic polymers were taken from the DSC data. The mass crystallinities of PCL1, PCL2 and PCL3 were determined according to the total enthalpy method [23] using calorimetric data from Refs. [24,25]: 85, 78 and 88%. This is similar to the crystallinity of linear PCL with a molar mass of 10 000 [26]. Hence, the higher diffusivities obtained for the dendritic PCL's cannot be explained by differences in the degree of crystallinity. A comparison of crystallinity data obtained by DSC and the measured densities (Table 1) indicates that the dendritic PCLs are microporous with the following porosities (for slabs): PCL1, 11%; PCL2, 3.5%; and PCL3, 4.2%. The absence of a two-stage desorption curve form indicates that the pores are discontinuous (Figs. 16 and 17).

The amorphous moisture solubility (volume fraction) may be calculated as:

$$S_{1a} = \nu_{2a}^{-1} S_1 \tag{30}$$

where ν_{2a} and S_1 are the volume fraction of amorphous polymer and the moisture content, respectively. Moisture solubility data (S_{1a}) are higher for the PCL1, PCL2 and PCL3 samples than for LPCL. The higher concentration of hydroxyl groups in the PCLx materials than in LPCL may also affect the moisture solubility. D_{co} values of the

Table 5
Moisture diffusivity and solubility data for PCLx and LPCL (obtained from desorption experiments)

Parameter	Sample PCL1	PCL2	PCL3	LPCL
D_{co} ($cm^2\ s^{-1}$)[a]	18.0×10^{-8}	7.0×10^{-8}	7.3×10^{-8}	$4.5\times10-8$[d]
α_D ($cm^3\ g^{-1}$)[a]	2	0.8	0.6	–
D_{co} ($cm^2\ s^{-1}$)[b]	0.9×10^{-6}	1.1×10^{-6}	1.2×10^{-6}	
α_D ($cm^3\ g^{-1}$)[b]	5	2.7	0.75	
S_{1a} ($g\ cm^{-3}$)[c]	0.031	0.021	0.032	0.011

[a] Obtained from PCL-slabs.
[d] From Ref. [13]
[b] Obtained from PCL-spheres.
[c] Moisture solubility in the amorphous component in gram solute per cm^3 polymer; average values of slab and sphere samples.

branched and the linear PCLs may be compared by using the Maxwell equation [27] to estimate the amorphous component diffusivity:

$$D_{coa} = D_{co}\frac{3 - \nu_{2a}}{2} \tag{31}$$

It was found that the amorphous component diffusivity was also higher in the dendritic polymers than in their linear analogue. The high moisture solubility and diffusivity of the dendritic polymers are well explained by their microporous character with a convective mass transport and adsorption of water molecules on the surfaces on the internal voids.

Information about the crystalline morphology of the dendritic PCLs was obtained from the DSC melting peak temperatures: PCL1, 323.0; PCL2, 329.1; and PCL3, 325.1 K. Using the Thomson–Gibbs equation (details of the derivation are provided by Gedde [28])

$$L_c = \frac{2\sigma_f T_m^0}{(T_m^0 - T_m)\Delta h_f^0 \rho_c} \tag{32}$$

it is possible to estimate crystal thicknesses (L_c) using the following data for linear PCL; σ_ε is the fold surface free energy (101 mJ m^{-2}[24]), T_m and T_m^0 are the experimental and equilibrium melting peak temperatures, respectively

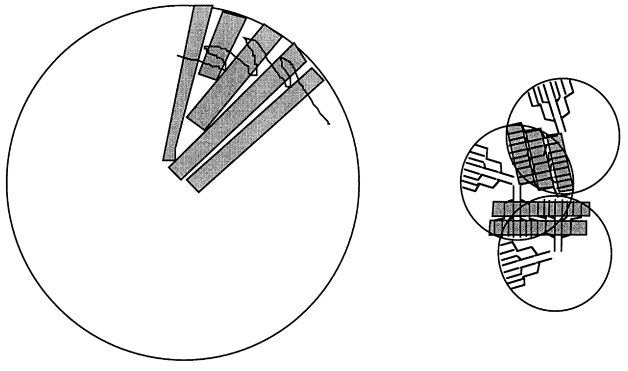

Fig. 18. A schematic drawing of a LPCL spherulite and the trajectory of three PCLx molecules with respect to the crystallites (grey areas).

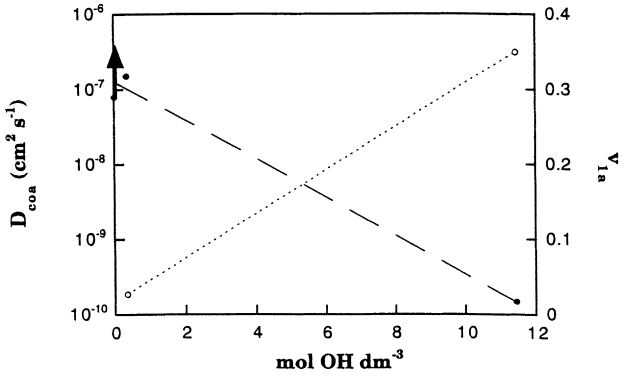

Fig. 19. Amorphous component zero concentration moisture diffusivity (●) and volume fraction of moisture at 100% relative humidity (○) as a function of polymer hydroxyl concentration. Data are averages for each material type (i.e. averages of data obtained for polymers of different generations). Since CAx diffusivity-data (no hydroxyl groups present) determined using the larger penetrant (ethylene glycol) represent data for the semicrystalline material, the use of water molecule as penetrant as well as considering only the diffusivity of the amorphous component should give higher diffusivities than reported. Therefore, there is an arrow pointing upward from the CA point in the figure.

($T_m^0 = 349.3$ K [24]) and Δh_f^0 is the heat of fusion for 100% crystalline polymer (155.9 kJ kg^{-1} [29]). The calculated crystal thicknesses are: PCL1, 14.5 nm; PCL2 18.8 nm; and 15.7 nm. If these values are compared with the length of the ε-caprolactone repeating unit (0.83 nm), it may be concluded that there is a crystalline stem consisting of 18, 23 and 19 repeating units for PCL1, PCL2 and PCL3, respectively. Since the degree of polymerization (DP) is between 20 and 21.5 per generation for all the PCLx materials, as was obtained by NMR, it may be concluded that the ε-caprolactone units are extended (Fig. 18). It is probable that a given crystal contains chain segments from several molecules and it is possible that straight 20 monomer units turn back and crystallize with the lower generation. Other important information was obtained by comparing the rates of degradation in chlorosulphonic acid of the dendritic and linear PCLs: PCL1, PCL2 and PCL3 degraded more rapidly than their linear counterpart, LPCL, although the former had a higher degree of crystallinity. This suggests that PCLx samples contained pores. The reason for the formation of pores (voids) in the dendritic PCLs polymers can only be speculated on. Crystallization certainly causes a volume decrease and the structural continuity (dendritic character) is likely to build up stresses that lead to void formation. Like the case of CAx's, films of PCL1 were prepared by compression moulding at high pressure to find out if PCLx's could be made pore-free. The densities of these films were close to that of LPCL ($\rho = 1146$–1148 kg cm^{-3}) which, by using the d.s.c. data, resulted in a porosity of 2%. Hence, it was impossible to eliminate all pores by applying an external pressure during crystallization.

The effect of the presence of hydrogen bonds on the solubility and diffusivity of small molecules is well illustrated in Fig. 19. Solubility increases drastically and zero concentration diffusivity decreases with increasing hydroxyl concentration. Even though the Cax's are semicrystalline and are in this case penetrated by a larger molecule, they possess larger diffusivities than the samples containing hydroxyl groups (HHx).

5. Conclusion

The sigmoidal sorption curves for the system moisture-hydroxyl-functional hyperbranched polymers were successfully modelled using Fick's equations with a time-dependent surface concentration where the time-dependence was determined from the mechanical stress relaxation data. Both the diffusivity data and the stress relaxation data indicated that these materials were plasticized by moisture. The zero concentration diffusivities were very small and comparable with the values for fully amorphous poly(vinyl alcohol). The replacement of the hydroxyl groups with C16 paraffin tails resulted in an increase in solute diffusivity despite the fact that these polymers became semicrystalline. The shape of the desorption curves indicated that continuous micropores were present and that these facilitated mass transport. The dendrimer-like star-shaped PCL's showed higher amorphous-polymer moisture solubilities and diffusivities than linear PCL. The low measured densities of these highly crystalline dendritic polymers confirmed a porosity which, according to the shape of the desorption curves, had to be discontinuous. It was impossible to eliminate all pores of either the C16-terminated or the PCLx materials by applying a high external pressure during crystallization. A collective view of all the results obtained confirms that the transport properties are primarily controlled by the hydroxyl group concentration.

Acknowledgements

The financial support from the Swedish Natural Science Research Council (NFR) grant K-AA/KU 01910-311, the Swedish Research Council for Engineering Sciences (TFR) grant 210:97–125, and the experimental assistance of A. Hellman, Packforsk-Swedish Packaging Research Institute, and Å. Johansson, Polymer Technology, Royal Institute of Technology, are gratefully acknowledged.

References

[1] Uhrich K. Trends Polym Sci 1997;5:388.
[2] Jansen JF, de Brabender-van der Berg E, Meijer E. Science 1994;266:1226.
[3] Jansen JF, Meijer E. J Am Chem Soc 1995;117:4417.
[4] Liu H, Uhrich K. Proc Am Chem Soc Div Polym Chem 1997;38:582.
[5] Duncan R, Malik N. Proc Int Symp Control Rel Bioact Mater 1996;23:105.
[6] Nielsen T. Active packaging, SIK Report, Gothenburg, Sweden, 1997.

[7] Malmström E, Johansson M, Hult A. Macromol Chem Phys 1996;197:3199.
[8] Hedenqvist M, Tränkner T, Johnsson G, Gedde UW. Polym Eng Sci 1995;36:4359.
[9] Hedenqvist M, Gedde UW. Polymer 1999;40:2381.
[10] Trollsås M, Hedrick JL. J Am Chem Soc 1998;4644.
[11] Crank J. The mathematics of diffusion, 2. Oxford: Clarendon Press, 1986.
[12] Bakhouya A, El Brouzi A, Bouzon J, Vergnaud JM. Plast Rubber Comp Proc Appl 1993;19:77.
[13] Fujita H. Fortshr Hochpol Forsch 1961;3:1.
[14] Hedenqvist MS, Ohrlander M, Palmgren R, Albertsson AC. Polym Eng Sci 1998;38:1313.
[15] Kahaner D, Moler C, Nash S. Numerical methods and software, Englewood Cliffs, NJ: Prentice-Hall, 1989.
[16] Becker GW. Kolloid Z 1961;175:99.
[17] Becker GW, Rademacher HJ. J Polym Sci, Polym Phys Ed 1962;58:621.
[18] Nisizawa M. J Appl Polym Sci 1969;13:1621.
[19] van Krevelen DW. Properties of polymers, 2. Amsterdam: Elsevier, 1976.
[20] Crank J, Park GS. Diffusion in polymers, Cambridge: Academic Press, 1968.
[21] Hedenqvist M, Angelstok A, Larsson PT, Edsberg LE, Gedde UW. Polymer 1996;37:2887.
[22] Khambata FB, Warner F, Russel T, Stein RS. J Polym Sci, Polym Phys Ed 1976;14:1391.
[23] Gray AP. Thermochim Acta 1970;1:563.
[24] Hoffman JD, Miller RL, Marand H, Roitman DB. Macromolecules 1992;25:2221.
[25] Wunderlich B. ATHAS Data Bank, University of Tennessee, Knoxville, TN, available at funnelweb.utcc.utk.edu.
[26] Krook M, Hedenqvist MS, Albertsson A-C, Hellman A, Iversen T, Gedde UW. Polym Eng Sci, in press.
[27] Progelhof PC, Throne JL, Ruetsch RR. Polym Eng Sci 1976;16:615.
[28] Gedde UW. Polymer physics, London: Chapman and Hall, 1995. 144 p.
[29] Lebedev B, Yevstropov A. Makromol Chem 1984;185:1235.